An analytical framework for locally resonant piezoelectric metamaterial plates

C. Sugino [a], M. Ruzzene [a,b], A. Erturk [a,*]

[a] G.W. Woodruff School of Mechanical Engineering, Georgia Institute of Technology, Atlanta, GA, USA
[b] D. Guggenheim School of Aerospace Engineering, Georgia Institute of Technology, Atlanta, GA, USA

ARTICLE INFO

ABSTRACT

We present an analytical modeling framework and its analysis for thin piezoelectric metamaterial plates to enable and predict low-frequency bandgap formation in finite structural configurations with specified boundary conditions. Using Hamilton's extended principle and the assumptions of classical (Kirchhoff) plate theory, the governing equations and boundary conditions for the fully coupled two-dimensional electromechanical system are obtained. The two surfaces of the piezoelectric bimorph are segmented into non-overlapping opposing pairs of electrodes of arbitrary shape, and each pair of electrodes is shunted to an external circuit. This formulation can be used to study the effect of electrode shape on plate response for topology optimization and other vibration control applications. Using modal analysis, we show that for a sufficient number of electrodes distributed across the surface of the plate, the effective dynamic stiffness of the plate is determined by the shunt circuit admittance applied to each pair of electrodes and the system-level electromechanical coupling. This enables the creation of locally resonant bandgaps and broadband attenuation, among other effects, in analogy with our previous work for one-dimensional piezoelectric structures with synthetic impedance shunt circuits. It is also demonstrated that piezoelectric bimorph plates display significantly improved performance (i.e. electromechanical coupling) over bimorph beams, but require additional electrode segmentation to achieve metamaterial-type performance. The governing equations are also used for dispersion analysis using the plane wave expansion method, enabling the analytical dispersion analysis of unit cells with arbitrary electrode shapes. The modeling framework and approximate closed-form bandgap expressions are numerically validated using finite element analysis.

1. Introduction

Piezoelectric materials have been used for a wide range of structural engineering applications, ranging from vibration control (Bailey and Hubbard, 1985; Hagood and von Flotow, 1991; Forward, 1979; Dosch et al., 1992; Arafa and Baz, 2000) to energy harvesting (Erturk and Inman, 2009). Using the piezoelectric effect, vibration can be dissipated with external circuitry, removing the need for bulky actuators or mass-based solutions. This concept of *piezoelectric shunt damping* has a rich history of research, covering topics from the use of negative capacitance shunt circuits (Tang and Wang, 2001; Park and Baz, 2005; De Marneffe and Preumont, 2008), to more general multi-mode damping circuits (Fleming et al., 2002; Niederberger et al., 2004) or distributed networks (Moheimani et al., 2004; Fleming and Moheimani, 2004; Preumont et al., 2008; Yu and Wang, 2009). More recently, these shunt damping concepts have been extended to elastic metamaterials (Casadei et al., 2010; Chen et al., 2014; Sugino et al., 2017; Chen et al., 2017; Li et al., 2018; Sugino et al., 2018), yielding rich dynamical behavior with attractive vibration attenuation properties, such as the formation of low-frequency vibrational bandgaps. By changing the shunt circuitry used with the metamaterial, the effective dynamic stiffness of the structure can be changed, giving unprecedented control over its dynamic performance. In our previous work, we derived the governing equations for a finite piezoelectric bimorph beam with segmented electrodes, deriving the effective stiffness of the bimorph beam, as well as the edge frequencies of the locally resonant bandgap. Such one-dimensional structures may not be viable for many structural applications, and so the goal of this work is to extend that one-dimensional analysis to a two-dimensional electromechanical metastructure (i.e metamaterial-based finite structure with specified boundary condi-

* Corresponding author.
  E-mail address: alper.erturk@me.gatech.edu (A. Erturk).

tions) consisting of a piezoelectric bimorph plate with segmented electrodes.

Piezoelectric plate vibration has been studied extensively in the literature (Mindlin, 1972; Lee, 1990; Dimitriadis et al., 1991; Mitchell and Reddy, 1995; Heyliger and Saravanos, 1995; Saravanos et al., 1997; He et al., 2001; Zhong and Shang, 2003; De Marqui et al., 2009; Tiersten, 2013). However, relatively little attention given to simplified models for thin bimorph plates, despite their applicability to a wide range of engineering systems. Analogous simplified theories for piezoelectric bimorph beams have been used extensively for studying vibrational energy harvesting (Erturk and Inman, 2009). Extensions to thin bimorph plates have generally considered a specific form of electrode segmentation, such as rectangular electrodes (Kim et al., 2005; Qiu et al., 2007; Aridogan et al., 2014), or specific plate geometries (Wang et al., 2001), but there is still need for more general models. For systems with a large number of segmented electrodes such as electromechanical metamaterial systems, irregular segmentation patterns may be significantly more practical, potentially enabling electrode lead access from the plate edges. Additionally, although some work has studied the unit-cell based analysis of infinite piezoelectric metamaterial plates (Sheng-Bing et al., 2013; Chen et al., 2014; Zhang et al., 2015), the effects of the finiteness of the structure and boundary conditions have not been directly accounted for. Here we present a theoretical framework applicable to piezoelectric bimorph plates with general segmentation into multiple electrodes of arbitrary shape, enabling the modal analysis of these structures as well as optimization of the electrode placement and shape. Using modal analysis, we demonstrate that the piezoelectric bimorph plate acts as an electromechanical metastructure for a sufficient number of electrodes placed across the surface of the plate. Furthermore, the effective electromechanical coupling of the plate is derived in terms of geometrical and material properties, and the effective dynamic stiffness of the plate is obtained. Numerical studies are performed to demonstrate the vibration attenuation performance of locally resonant electromechanical metamaterial plates, and the effect of the number and placement of electrodes is explored. Using the developed equations, unit-cell based dispersion analysis is performed using the plane wave expansion method. To validate the results, finite element simulations were performed in COMSOL Multiphysics for a thin locally resonant bimorph plate and compared with the developed theory.

2. Piezoelectric bimorph locally resonant metamaterial plate

Consider a thin piezoelectric bimorph plate made from two continuous and symmetrically located piezoelectric layers sandwiching a central isotropic layer (i.e. shim). The piezoelectric layers are poled in the same direction through the thickness for parallel operation under transverse vibrations, and the central shim is assumed to be an ideal conductor. The shim has thickness h_s, Young's modulus E_s, Poisson's ratio v_s, and density ρ_s. For simplicity, only the case of transversely isotropic piezoelectric materials (e.g., piezoceramics) will be considered here. Orthotropic piezoelectric materials can be considered under a similar modeling framework using Hamilton's principle. The piezoelectric layers are assumed to have the same material properties, with identical thickness h_p and density ρ_p, and constitutive law given as described in Appendix A, with effective stiffness coefficients at constant electric field $\bar{c}_{11}^E$, $\bar{c}_{12}^E$, $\bar{c}_{66}^E$, piezoelectric coupling $\bar{e}_{31}$, and permittivity at constant strain $\bar{\varepsilon}_{33}^S$, given respectively as

$$\bar{c}_{11}^E = \frac{s_{11}^E}{\left(s_{11}^E + s_{12}^E\right)\left(s_{11}^E - s_{12}^E\right)} \tag{1}$$

$$\bar{c}_{12}^E = \frac{-s_{12}^E}{\left(s_{11}^E + s_{12}^E\right)\left(s_{11}^E - s_{12}^E\right)} \tag{2}$$

$$\bar{c}_{66}^E = \frac{1}{s_{66}^E} = \frac{1}{2}\left(\bar{c}_{11}^E - \bar{c}_{12}^E\right) \tag{3}$$

$$\bar{e}_{31} = \frac{d_{31}}{s_{11}^E + s_{12}^E} \tag{4}$$

$$\bar{\varepsilon}_{33}^S = \varepsilon_{33}^T - \frac{2d_{31}^2}{s_{11}^E + s_{12}^E} \tag{5}$$

where the overbars indicate properties obtained from the full constitutive equations under the assumptions of plane stress and voltage applied through the thickness. A representative schematic of the plate is shown in Fig. 1.

2.1. Governing equations

Under the assumptions of Kirchhoff-Love plate theory and using Hamilton's principle (see Appendix B for the full derivation), the governing equations for transverse vibrations can be obtained as

$$D^E \nabla^4 w(\mathbf{P}, t) + m_p \frac{\partial^2 w(\mathbf{P}, t)}{\partial t^2} - \vartheta \nabla^2 v(\mathbf{P}, t) = f(\mathbf{P}, t), \quad \mathbf{P} \in D \tag{6}$$

$$\hat{C}_p \frac{\partial v(\mathbf{P}, t)}{\partial t} + \vartheta \frac{\partial}{\partial t} \nabla^2 w(\mathbf{P}, t) = J(\mathbf{P}, t), \quad \mathbf{P} \in D \tag{7}$$

where $w(\mathbf{P}, t)$ is the transverse displacement at a point $\mathbf{P}$ in the two-dimensional domain D at time t, $v(\mathbf{P}, t)$ is the voltage between the surface of the piezoelectric layers and the central shim, D^E is the effective flexural rigidity of the plate at constant electric field (i.e. short circuit), m_p is the mass per area of the plate, ϑ is the coupling parameter in physical coordinates, and $\hat{C}_p$ is the piezoelectric capacitance per area, given respectively as

$$D^E = D_s + D_p \tag{8}$$

$$m_p = \rho_s h_s + 2\rho_p h_p \tag{9}$$

$$\vartheta = \bar{e}_{31}(h_s + h_p) \tag{10}$$

$$\hat{C}_p = \frac{2\bar{\varepsilon}_{33}^S}{h_p} \tag{11}$$

where D_s and D_p are the flexural rigidity contributions from the structural layer and piezoelectric layers respectively, given by

$$D_s = \frac{E_s h_s^3}{12\left(1 - v_s^2\right)}, \quad D_p = \bar{c}_{11}^E\left(\frac{1}{6}h_p\left(4h_p^2 + 6h_p h_s + 3h_s^2\right)\right) \tag{12}$$

Furthermore, $f(\mathbf{P}, t)$ is the external loading applied to the plate, and $J(\mathbf{P}, t)$ is the external current density field flowing out of the external surfaces of the piezoelectric layers and into the central shim. Eqs. (6) and (7) apply for points $\mathbf{P}$ within a two-dimensional domain D, which has a continuous one-dimensional boundary ∂D. Note that no assumptions have been made regarding the voltage field $v(\mathbf{P}, t)$, which is allowed to vary freely in the domain D. The coupling through the Laplacian operator in Eq. (6) can be interpreted as the in-plane force resulting from voltage applied to the piezoelectric layers operating in the 3-1 mode.

The use of Hamilton's principle immediately yields the boundary conditions for the fully coupled problem as
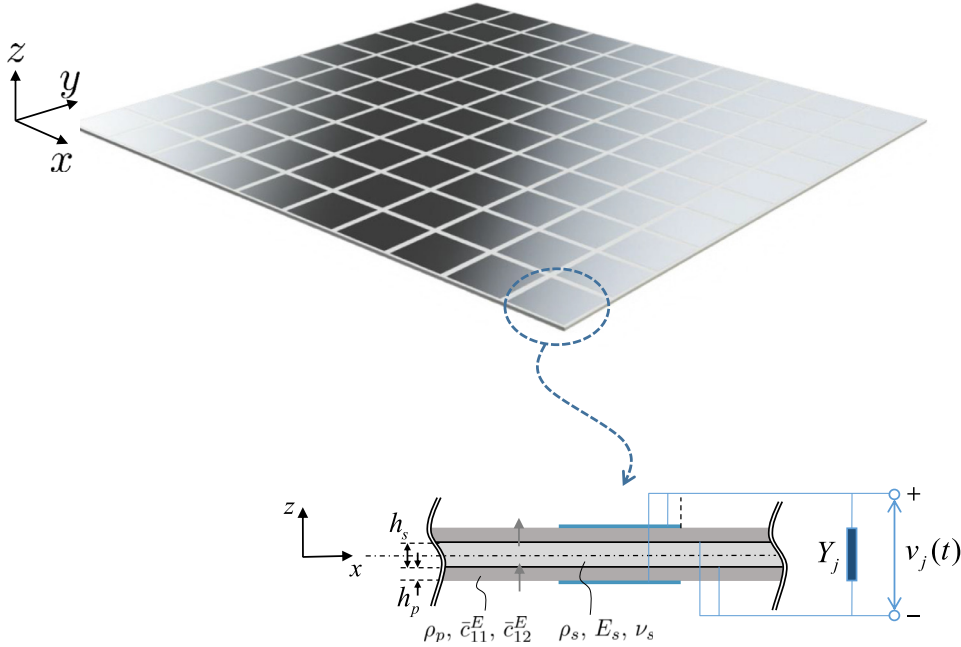
Fig. 1. Schematic of the bimorph plate showing a cross section and single electrode. Note that the plate geometry, coordinate system, and electrode shapes are all arbitrary, and are only shown here for illustration.

either $\quad w = 0 \quad$ or $\quad \dfrac{\partial}{\partial s} M_{ns} - D^E \dfrac{\partial}{\partial n} \nabla^2 w + \vartheta \dfrac{\partial v}{\partial n} = 0 \quad$ on $\quad \partial D$

$$\text{(13a)}$$

and

either $\quad \dfrac{\partial w}{\partial n} = 0 \quad$ or $\quad M_n + \vartheta v = 0 \quad$ on $\quad \partial D$ $\qquad$ (13b)

where

$$M_n = -D^E \nabla^2 w + D^E (1 - v) \left(\frac{\partial^2 w}{\partial s^2} + \frac{1}{R} \frac{\partial w}{\partial n} \right) \qquad (14)$$

$$M_{ns} = -D^E (1 - v) \frac{\partial^2 w}{\partial n \partial s} \qquad (15)$$

where n and s denote the normal and tangential directions to the boundary, R is the local radius of curvature on the boundary, and v is a term analogous to the Poisson's ratio of the bimorph, given by

$$v = \frac{D_s v_s + D_p v_p}{D^E} \qquad (16)$$

where

$$v_p = \frac{\bar{c}^E_{12}}{\bar{c}^E_{11}} = -\frac{s^E_{12}}{s^E_{11}} \qquad (17)$$

is the effective Poisson's ratio of the transversely isotropic piezoelectric layers. The Laplacian operator in normal and tangential coordinates is given by

$$\nabla^2 = \frac{\partial^2}{\partial n^2} + \frac{1}{R} \frac{\partial}{\partial n} + \frac{\partial^2}{\partial s^2} \qquad (18)$$

Additionally, the "corner condition" encountered in plate boundary value problems must be satisfied, i.e.

$$M_{ns} \delta w \big|_{\partial D} = 0 \qquad (19)$$

either explicitly or implicitly. Note that both natural boundary conditions are altered by the coupling between the displacement and voltage fields. In principle these equations can be used to solve for the exact solutions to the fully coupled boundary value problem formed by Eqs. (6) and (7), along with the boundary conditions Eqs. (13a) and (13b). However, note that when both surfaces of the bimorph are short circuited to the central shim, $v(\mathbf{P}, t) = 0$, Eq. (6) simplifies to the classical plate vibration equation, and both Eqs. (13a) and (13b) immediately simplify to typical plate boundary conditions Meirovitch (1997). In the following, it is assumed that the resulting short-circuit boundary value problem has been solved for the short-circuit mode shapes $\phi_r(\mathbf{P})$ and natural frequencies ω_r, and that the mode shapes are normalized to satisfy the orthogonality conditions

$$\int_D m_p \phi_r(\mathbf{P}) \phi_s(\mathbf{P}) dD = \delta_{rs}, \quad r, s = 1, 2, \ldots \qquad (20)$$

$$\int_D D^E \phi_r(\mathbf{P}) \nabla^4 \phi_s(\mathbf{P}) dD = \omega_r^2 \delta_{rs}, \quad r, s = 1, 2, \ldots \qquad (21)$$

These solutions are readily available in the literature for a wide variety of boundary conditions and plate geometries, but the following analysis is fully general and does not rely on closed-form expressions for the mode shapes or natural frequencies.

2.2. Short and open circuit conditions

Both short circuit and open circuit conditions are easily investigated from the form of the governing equations in Eqs. (6) and (7). Short circuit corresponds to the case $v(\mathbf{P}, t) = 0$, such that Eq. (6) becomes

$$D^E \nabla^4 w(\mathbf{P}, t) + m_p \frac{\partial^2 w(\mathbf{P}, t)}{\partial t^2} = f(\mathbf{P}, t), \quad \mathbf{P} \in D \qquad (22)$$

which is the typical field equation for a uniform plate in bending (see e.g. Meirovitch (1997)). In the case of open circuit, no additional external current can flow through the piezoelectric material, and so $J(\mathbf{P}, t) = 0$. In this case, Eq. (7) can be substituted into

Eq. (6) to obtain

$$D^E(1+\alpha)\nabla^4 w(\mathbf{P},t) + m_p \frac{\partial^2 w(\mathbf{P},t)}{\partial t^2} = f(\mathbf{P},t), \quad \mathbf{P} \in D \qquad (23)$$

which again is the typical field equation for a uniform plate in bending, where

$$\alpha = \frac{\vartheta^2}{D^E \hat{C}_p} \qquad (24)$$

is a dimensionless term that gives the system-level electromechanical coupling, which relates the short-circuit (constant electric field) flexural rigidity D^E to the open-circuit (constant electric displacement) flexural rigidity D^D, given by

$$D^D = D^E(1+\alpha) \qquad (25)$$

Note that the open-circuit voltage field $v^D(\mathbf{P},t)$ can be recovered from the open-circuit displacement field as

$$v^D(\mathbf{P},t) = -\frac{\vartheta}{\hat{C}_p}\nabla^2 w(\mathbf{P},t) \qquad (26)$$

Importantly, this scenario is distinct from the commonly encountered case of surface electrodes being left at open circuit, since the voltage varies continuously across the surface of the plate. Additionally, it should be noted that, although the governing equation for open circuit (Eq. (23)) is identical to the governing equation for the classical plate boundary value problem, the boundary conditions are altered by the voltage coupling to the structure. Namely, substituting Eq. (26) into Eqs. (13a) and (13b) yields

either $w = 0$ or

$$-D^E(1-\nu)\frac{\partial^3 w}{\partial n \partial^2 s} - D^D\frac{\partial}{\partial n}\nabla^2 w = 0 \text{ on } \partial D \qquad (27a)$$

and

either $\dfrac{\partial w}{\partial n} = 0$ or

$$-D^D\nabla^2 w + D^E(1-\nu)\left(\frac{\partial^2 w}{\partial s^2} + \frac{1}{R}\frac{\partial w}{\partial n}\right) = 0 \text{ on } \partial D$$

$$(27b)$$

Thus, it is insufficient to simply replace the short circuit flexural rigidity D^E with the open circuit flexural rigidity D^D in the boundary conditions of the plate. This may or may not change the actual boundary conditions, depending on the plate geometry and type of boundary being considered. Clearly, systems with purely geometric boundary conditions would be unaffected, but certain natural boundary conditions are unchanged as well. For example, a simply supported edge of a rectangular plate at open circuit would still yield boundary conditions

$$w = 0, \quad \frac{\partial^2 w}{\partial n^2} = 0$$

which are identical to the typical simply supported boundary conditions. However, this will not generally be the case, and the change in boundary conditions may affect the perceived coupling factor, typically measured via the change in resonant frequencies from short to open circuit.

2.3. Governing equations for segmented electrodes

Control authority over the plate response comes via the external current density $J(\mathbf{P}, t)$. In a real structure, this current cannot be varied continuously in space over the domain D, and so it becomes necessary to segment the surfaces of the piezoelectric bimorph into pairs of opposing electrodes. Each elctrode is assumed to have a constant voltage over its surface and a uniform (i.e. lumped) current density. Thus, we assume a voltage field of the form

$$v(\mathbf{P},t) = \sum_{j=1}^{S} v_j(t) d_j(\mathbf{P}) \qquad (28)$$

where $v_j(t)$ is the voltage between the jth electrode pair and the central shim,

$$d_j(\mathbf{P}) = \begin{cases} 1, & \mathbf{P} \in D_j \\ 0, & \text{otherwise} \end{cases} \qquad (29)$$

is a step-type function identifying the region of the jth electrode, $D_j \subseteq D$ is the subdomain corresponding to the jth electrode, and S is the total number of electrodes. Due to the assumption of parallel wire operation, each electrode in a pair of opposing electrodes has the same voltage level referenced to the central shim. Eq. (28) requires both surfaces of the piezoelectric material to be short-circuited wherever there are no electrodes, resulting in voltage discontinuities at the boundary of each electrode. As such, Eq. (28) is an approximation, but it provides significant simplifications in the following analysis. Higher order models could account for larger open-circuit regions or smooth voltage transitions between electrodes, but this is beyond the scope of this work. Additionally, the accuracy of the approximation in Eq. (28) will be evaluated through comparison with finite element results.

Substituting Eq. (28) into Eq. (7) and integrating over the jth electrode D_j yields

$$C_{p,j}\dot{v}_j(t) + \mathscr{Y}_j\big[v_j(t)\big] + \vartheta\frac{\partial}{\partial t}\int_{D_j}\nabla^2 w(\mathbf{P},t)dD = 0, \quad j = 1\ldots S$$

$$(30)$$

where $C_{p,j}$ is the effective capacitance of the jth electrode pair, given by

$$C_{p,j} = \hat{C}_p \Delta D_j = \int_{D_j} \hat{C}_p dD \qquad (31)$$

where ΔD_j is the area of the jth electrodes, and it has been assumed that

$$\int_{D_j} J(\mathbf{P},t)dD = -\mathscr{Y}_j\big[v_j(t)\big] \qquad (32)$$

i.e. that the external current into the jth electrode is due to a lumped admittance $\mathscr{Y}_j$ acting on the voltage of the electrode $v_j(t)$.

To discretize the transverse displacement field, we assume a modal expansion of the form

$$w(\mathbf{P},t) = \sum_{r=1}^{N}\phi_r(\mathbf{P})\eta_r(t) \qquad (33)$$

where $\phi_r(\mathbf{P})$ are the mass-normalized (see Eqs. (20) and (21)) short-circuit mode shapes, $\eta_r(t)$ are the modal coordinates to be determined, and N is the total number of modes used in the expansion. Substituting Eqs. (28) and (33) into Eq. (6), multiplying by some mode shape $\phi_r(\mathbf{P})$ and integrating over the entire domain D gives

$$\ddot{\eta}_r(t) + \omega_r^2\eta_r(t) - \vartheta\sum_{j=1}^{S}v_j(t)\int_D\phi_r(\mathbf{P})\nabla^2 d_j(\mathbf{P})dD = q_r(t) \qquad (34)$$

where

$$q_r(t) = \int_D f(\mathbf{P},t)\phi_r(\mathbf{P})dD \qquad (35)$$

is the rth modal excitation. Substituting Eq. (33) into Eq. (30) gives

$$C_{p,j}\dot{v}_j(t) + \mathscr{Y}_j\big[v_j(t)\big] + \vartheta\sum_{r=1}^{N}\dot{\eta}_r(t)\Gamma_{r,j} = 0 \qquad (36)$$

where

$$\Gamma_{r,j} = \int_D d_j(\mathbf{P})\nabla^2\phi_r(\mathbf{P})dD = \int_{D_j} \nabla^2\phi_r(\mathbf{P})dD \tag{37}$$

is the coupling between the rth mode shape and the jth voltage. To obtain symmetric coupling between the two equations, we use the identity

$$\phi_r\nabla^2 d_j = \nabla\cdot\left(\phi_r\nabla d_j - d_j\nabla\phi_r\right) + d_j\nabla^2\phi_r \tag{38}$$

such that the integral in Eq. (34) becomes

$$\int_D \phi_r(\mathbf{P})\nabla^2 d_j(\mathbf{P})dD = \Gamma_{r,j} + \oint_{\partial D}\left(\phi_r(\mathbf{P})\nabla d_j(\mathbf{P}) - d_j(\mathbf{P})\nabla\phi_r(\mathbf{P})\right)\cdot\mathbf{n}dS \tag{39}$$

where the divergence theorem has been used to obtain the boundary integral, whose path is oriented to be aligned with the transverse axis by the right hand rule. This boundary integral will vanish under the condition that either (1) purely geometric boundary conditions apply or (2) the voltage vanishes at the boundaries (i.e. that no electrodes are placed on the boundary). Otherwise, any nonzero voltage on the boundary exerts a moment or effective shear that will affect the boundary conditions of the plate. Here, we assume the voltage and its normal derivative go to zero at the boundary, or that electrodes are not placed directly on the boundary of the plate. Boundary-adjacent electrodes may be handled more thoroughly by accounting for them in the original mode shapes used as basis functions, in which case the symmetric form of the orthogonality integral Eq. (21) must be altered to include the boundary electrodes.

Assuming that the boundary integral vanishes, the discretized governing equations can be summarized as

$$\ddot{\eta}_r(t) + \omega_r^2\eta_r(t) - \vartheta\sum_{j=1}^S v_j(t)\Gamma_{r,j} = q_r(t), \quad r = 1\ldots N \tag{40}$$

$$C_{p,j}\dot{v}_j(t) + \mathscr{Y}_j\left[v_j(t)\right] + \vartheta\sum_{r=1}^N \dot{\eta}_r(t)\Gamma_{r,j} = 0, \quad j = 1\ldots S \tag{41}$$

For a specified set of shunt admittances $\mathscr{Y}_j$ and electrode shapes D_j, Eqs. (40) and (41) can be solved using typical ordinary differential equation techniques. Note that the coupling between the two equations takes the form of an integral that depends on the electrode shapes D_j which must be computed to solve the fully coupled problem. For electrodes with smoothly parameterized boundaries (e.g., circular electrodes), it may be simpler to use the alternate form

$$\Gamma_{r,j} = \int_{D_j}\nabla^2\phi_r(\mathbf{P})dD = \oint_{\partial D_j}\nabla\phi_r(\mathbf{P})\cdot\mathbf{n}\,ds \tag{42}$$

which can be computed numerically as integration over a single variable.

Taking the Laplace transform of Eqs. (40) and (41) and substituting Eq. (41) into (40) yields

$$(s^2 + \omega_r^2)H_r(s) + \frac{\alpha s}{s + h(s)}\sum_{k=1}^N H_k(s)\sum_{j=1}^S \frac{D^E}{\Delta D_j}\Gamma_{k,j}\Gamma_{r,j} = Q_r(s) \tag{43}$$

where

$$h(s) = \frac{Y_j(s)}{C_{p,j}} \tag{44}$$

is a normalized version of the shunt circuit admittance, assumed to be identical for every pair of electrodes, $Y_j(s)$ is the Laplace transform of $\mathscr{Y}_j$ (i.e. the shunt admittance in the Laplace domain), and α is the dimensionless electromechanical coupling term given by

Eq. (24). Since the mode shapes are continuous, application of the mean value theorem yields

$$\frac{\Gamma_{r,j}}{\Delta D_j} = \frac{1}{\Delta D_j}\int_{D_j}\nabla^2\phi_r(\mathbf{P})dD = \nabla^2\phi_r(\mathbf{P}_{r,j}), \quad \mathbf{P}_{r,j} \in D_j \tag{45}$$

where the point $\mathbf{P}_{r,j}$ depends on the mode and electrode being considered and may not be unique. Note that in practice it is much simpler to calculate the left hand side of this equation, rather than find the specific point $\mathbf{P}_{r,j}$. Thus,

$$(s^2 + \omega_r^2)H_r(s) + \frac{\alpha s}{s + h(s)}\sum_{k=1}^N H_k(s)\sum_{j=1}^S D^E\nabla^2\phi_r(\mathbf{P}_{r,j})$$
$$\nabla^2\phi_k(\mathbf{P}_{k,j})\Delta D_j = Q_r(s) \tag{46}$$

Eq. (46) is a system of N linear equations that can be solved numerically for the modal response for a given excitation. However, note that in the limit as the number of electrodes approaches infinity, the points $\mathbf{P}_{r,j}$ and $\mathbf{P}_{k,j}$ collapse to the same point, and

$$\lim_{S\to\infty}\sum_{j=1}^S D^E\nabla^2\phi_r(\mathbf{P}_{r,j})\nabla^2\phi_k(\mathbf{P}_{k,j})\Delta D_j = \int_D D^E\nabla^2\phi_r(\mathbf{P})\nabla^2\phi_k(\mathbf{P})dD = \omega_r^2\delta_{rk} \tag{47}$$

i.e., the summation forms a Riemann sum of the symmetric form of the orthogonality integral in Eq. (21), and hence the system of equations decouples. In this case, the modal response can be solved for in closed form

$$\frac{H_r(s)}{Q_r(s)} = \frac{1}{s^2 + \omega_r^2\left(1 + \dfrac{\alpha s}{s + h(s)}\right)} \tag{48}$$

which is identical to the expression obtained for piezoelectric bimorph beams in Sugino et al. (2017), although both α and $h(s)$ have slightly different forms. Since Eq. (48) holds for every mode of the structure, it is clear that the effective dynamic stiffness of the structure is given by

$$\frac{\bar{D}(s)}{D^E} = 1 + \frac{\alpha s}{s + h(s)} \tag{49}$$

where $\bar{D}(s)$ is the effective dynamic flexural rigidity of the metastructure. Note that at open circuit, $h(s) = 0$, and we recover $\bar{D}(s) = D^D = D^E(1 + \alpha)$. For real systems with a finite number of electrodes, it is necessary to check that the approximation

$$\sum_{j=1}^S D^E\nabla^2\phi_r(\mathbf{P}_{r,j})\nabla^2\phi_k(\mathbf{P}_{k,j})\Delta D_j \approx \int_D D^E\nabla^2\phi_r(\mathbf{P})\nabla^2\phi_k(\mathbf{P})dD \tag{50}$$

is satisfied in the frequency range of interest.

2.4. Electromechanical coupling

The system-level electromechanical coupling α is vital for understanding the performance of piezoelectric bimorph plates, as it determines the passively realizable variation of the effective stiffness of the structure. Expanding Eq. (24), the electromechanical coupling can be written in terms of dimensionless quantities as

$$\alpha = (k^p)^2\left(\frac{6\hat{h}(\hat{h}+1)^2}{\gamma + 2\hat{h}(4\hat{h}^2 + 6\hat{h} + 3)}\right) \tag{51}$$

where

$$\gamma = \frac{E}{\bar{c}_{11}^E(1 - \nu_s^2)}, \quad \hat{h} = \frac{h_p}{h_s}, \quad (k^p)^2 = \frac{\bar{e}_{31}^2}{\bar{\varepsilon}_{33}^S\bar{c}_{11}^E} \tag{52}$$

are dimensionless terms giving the stiffness ratio, thickness ratio, and the piezoelectric planar radial electromechanical coupling coefficient respectively. Note that the planar radial electromechanical coupling coefficient can be related to other commonly encountered electromechanical coupling coefficients as

$$(k^p)^2 = \frac{k_p^2(1+\nu_p)}{2(1-k_p^2)} = \frac{k_{31}^2(1+\nu_p)}{1-\nu_p-2k_{31}^2} \tag{53}$$

where k_p^2 is the planar electromechanical coupling coefficient, and k_{31}^2 is the extensional mode coupling factor. The system-level coupling α can be maximized at a given value of γ by satisfying

$$\gamma = \frac{4\hat{h}^3}{1+3\hat{h}} \tag{54}$$

although more typically Eq. (54) is solved for the optimal $\hat{h}$ for a certain value of γ, since γ is determined solely by the material properties of the central shim and piezoelectric layers. The corresponding maximum value of α for a given thickness ratio $\hat{h}$ is

$$\alpha_{opt}(\hat{h}) = (k^p)^2 \left(\frac{(\hat{h}+1)(3\hat{h}+1)}{(2\hat{h}+1)^2} \right) \tag{55}$$

such that the maximum value of α across its entire parameter space is

$$\alpha_{max} = (k^p)^2 \tag{56}$$

These material properties are readily available for piezoceramics (e.g., PZT-5A or PZT-5H), making it straightforward to evaluate α for any particular plate design. Interestingly, the plate model predicts a much larger value of α than the beam model developed in Sugino et al. (2017), which predicted a maximum value of

$$\alpha_{max,beam} = \frac{k_{31}^2}{1-k_{31}^2} = \frac{\alpha_{max}(1-\nu_p)}{(1+\nu_p)(1+\alpha_{max})} < \alpha_{max} \tag{57}$$

Even neglecting the Poisson effect, the coupling predicted in Sugino et al. (2017) is always smaller than the value predicted here. For reference, for PZT-5H the maximum value of α predicted in Sugino et al. (2017) is 0.178, whereas the maximum value predicted here is 0.478. Note however that the plate-type system requires additional electrode segmentation to achieve convergence to Eq. (50).

2.5. Locally resonant bandgap

Since the form of Eq. (48) is identical to the form presented in Sugino et al. (2017) and Sugino et al. (2018), the analysis in those works applies identically to the system considered here. In summary, the locally resonant bandgap can be obtained by using purely inductive shunt circuits, yielding normalized admittance

$$h(s) = \frac{\omega_t^2}{s} \tag{58}$$

where ω_t is the resonant frequency of the LC shunt circuit. With this type of shunt circuit, the effective modal response is given by

$$\frac{H_r(s)}{Q_r(s)} = \frac{1}{s^2 + \omega_r^2 \left(1 + \frac{\alpha s^2}{\omega_t^2 + s^2} \right)} \tag{59}$$

The effective dynamic flexural rigidity of the system is then

$$\frac{\bar{D}(s)}{D^E} = 1 + \frac{\alpha s^2}{\omega_t^2 + s^2} \tag{60}$$

which becomes negative in the frequency range

$$\frac{\omega_t}{\sqrt{1+\alpha}} < \omega < \omega_t \tag{61}$$

Table 1
Geometric and material properties for the plate considered in Section 2.6. The plate is rectangular with dimensions $a \times b$, an aluminum central shim, and PZT-5H as the piezoelectric material.

Parameter	Value	Parameter	Value
h_s	1 mm	h_p	1mm
ρ_s	2700 kg/m^3	ρ_p	7500 kg/m^3
E	68.9 GPa	$\bar{c}_{11}^E$	66.2 GPa
ν_s	0.33	ν_p	0.29
a	80 cm	$\bar{\varepsilon}_{33}^S$	17.29 nF/m
b	70 cm	$\bar{e}_{31}$	-23.38 C/m

which defines the locally resonant bandgap. Unlike a typical antiresonance, the locally resonant bandgap is characterized by a wide range of relatively constant vibration attenuation, associated with the effective dynamic stiffness becoming negative. The exception to this is at $s = j\omega_t$, an antiresonance that is present for every mode of the structure, yielding zero vibration amplitude everywhere on the plate.

2.6. Finite number of electrodes

For real systems with a finite number of electrodes, the approximation of Eq. (50) is never fully satisfied. However, for a large number of electrodes placed throughout the surface of the plate, we can observe good convergence to the infinite-electrode type performance.

For simplicity, we consider a simply supported rectangular plate of dimensions $a \times b$ in the x and y directions respectively. The mass-normalized mode shapes of a rectangular simply supported plate are

$$\phi_{mn}(x,y) = \frac{2}{\sqrt{m_p ab}} \sin\left(\frac{m\pi x}{a}\right) \sin\left(\frac{n\pi y}{b}\right) \tag{62}$$

with corresponding natural frequencies

$$\omega_{mn} = \pi^2 \left[\left(\frac{m}{a}\right)^2 + \left(\frac{n}{b}\right)^2 \right] \sqrt{\frac{D^E}{m_p}} \tag{63}$$

This modeling framework can be used to study performance for arbitrary electrode shapes by appropriate evaluation of the coupling integral of Eq. (42); however, for simplicity, only the case of rectangular electrodes is considered here. For rectangular electrodes spanning a region $x_j^L < x < x_j^R$, $y_j^L < y < y_j^R$, with dimensions $\Delta x_j = x_j^R - x_j^L$ and $\Delta y_j = y_j^R - y_j^L$, the coupling integral in Eq. (42) is given by

$$\Gamma_{mn,j} = -\frac{2\pi^2 \Delta D_j (b^2 m^2 + a^2 n^2)}{a^2 b^2 \sqrt{m_p ab}} \,\text{sinc}\left(\frac{m\pi \Delta x_j}{2a}\right) \text{sinc}\left(\frac{n\pi \Delta y_j}{2b}\right)$$
$$\times \sin\left(\frac{m\pi(x_j^L + x_j^R)}{2a}\right) \sin\left(\frac{n\pi(y_j^L + y_j^R)}{2b}\right) \tag{64}$$

where $\Delta D_j = \Delta x_j \Delta y_j$ is the area of the electrode, and the sinc function is defined as

$$\text{sinc}\, x = \begin{cases} 1 & x = 0 \\ \dfrac{\sin x}{x} & \text{otherwise} \end{cases} \tag{65}$$

In the remainder of this section, geometric and material parameters as described in Table 1 will be used, with PZT-5H as the piezoelectric material and an aluminum shim. For these dimensions and materials, the predicted value of the dimensionless coupling is $\alpha = 0.422$.

First, the response of a locally resonant bimorph plate with a specific set of electrodes is investigated. The transmissibility FRF for a plate with a uniform 10×10 grid of rectangular electrodes
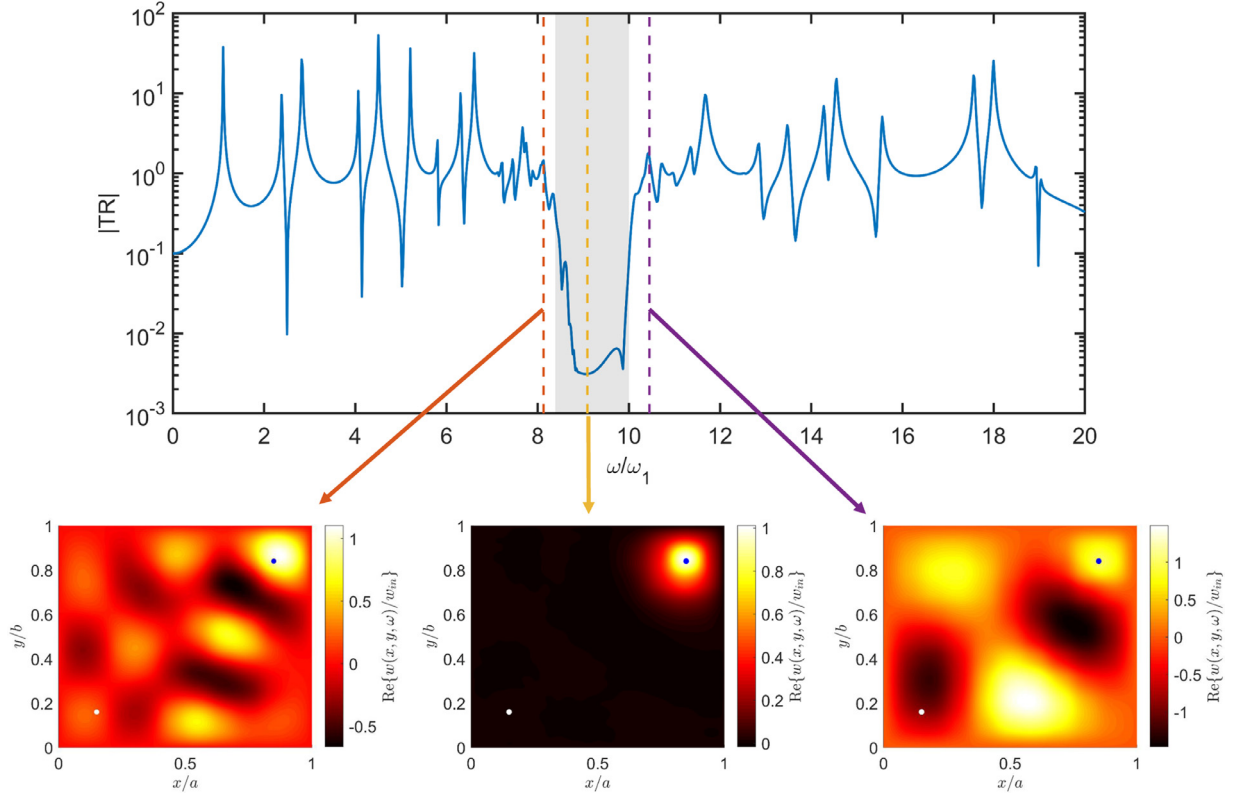
Fig. 2. Transmissibility between input at $(x, y) = (0.85a, 0.84b)$ and output at $(x, y) = (0.15a, 0.16b)$ for a simply supported bimorph plate with parameters as given in Table 1. The target frequency is $10\omega_1$, 0.5% damping was added to each shunt, and the locally resonant bandgap predicted by Eq. (61) is shown by the shaded gray region. The insets show the real part of the transverse displacement for the entire plate for frequencies before, inside, and after the bandgap ($\omega/\omega_1 = 8.13$, 9.09, and 10.45, respectively). In each inset, the input force location is shown by a blue circle, and the output is shown by a white circle. (For interpretation of the references to colour in this figure legend, the reader is referred to the web version of this article.)

and a target frequency of $\omega_t = 10\omega_1$ is shown in Fig. 2. There is excellent agreement between the observed locally resonant bandgap and the edge frequencies predicted by Eq. (61).

Next, to investigate the influence of the number of resonators on the plate response, we assume a square grid of electrodes with $S_x = S_y$ electrodes along each plate edge. Note that in general $S_x = S_y$ may not be required for convergence to Eq. (50), depending on the plate geometry and boundary conditions, but this assumption provides a straightforward technique to evaluate performance. With this assumption, the plate response can be computed as a function of $S_x = S_y$ for a specified target frequency ω_t. These results are shown in Fig. 3 for $\omega_t = 5\omega_1$, $10\omega_1$, and $20\omega_1$. There is clear convergence to the expected bandgap as the number of electrodes becomes sufficiently large in all cases, but more electrode segmentation is required to create the bandgap at high frequencies. This type of analysis can be used to study the performance of other combinations of electrode shape, plate boundary conditions, and plate shapes (e.g., circular plates).

3. Dispersion calculation using the plane wave expansion method

The governing equations derived in Section 2 can also be used for unit-cell based dispersion analysis using the plane wave expansion (PWE) method. Assuming a two-dimensional Bravais lattice of unit cells with lattice vectors $\boldsymbol{a}_1$ and $\boldsymbol{a}_2$ and harmonic excitation at a frequency ω, Eqs. (6) and (30) become

$$\left(D^E \nabla^4 - m_p \omega^2\right)\bar{w}(\mathbf{P}, j\omega) - \vartheta \sum_{r,s} \bar{v}_{rs} \nabla^2 d(\mathbf{P} - \mathbf{P}_{rs}) = 0 \quad (66)$$

$$(j\omega C_p + Y(j\omega))\bar{v}_{rs} + j\omega\vartheta \int_D d(\mathbf{P} - \mathbf{P}_{rs})\nabla^2\bar{w}(\mathbf{P}, j\omega)dD = 0 \quad (67)$$

where $\bar{w}(\mathbf{P}, j\omega)$ is the transverse displacement amplitude at a point $\boldsymbol{P}$ and frequency ω, $\mathbf{P}_{rs} = r\mathbf{a}_1 + s\mathbf{a}_2$ denotes the position of the origin of the unit cell at lattice coordinates (r, s) for $r, s \in \mathbb{Z}$, $\bar{v}_{rs}$ is the voltage on the electrode at unit cell (r, s), and $d(\boldsymbol{P})$ is the electrode shape function (see Eq. (29)) defined for the unit cell $(0, 0)$. To use the plane wave expansion method, we assume a displacement field of the form

$$\bar{w}(\mathbf{P}, j\omega) = \sum_{m,n} W(\mathbf{G}_{mn}, j\omega)e^{-j(\mathbf{k}+\mathbf{G}_{mn})\cdot\mathbf{P}} \quad (68)$$

where $\mathbf{G}_{mn} = m\mathbf{b}_1 + n\mathbf{b}_2$ is the (m, n) reciprocal lattice point, where $\boldsymbol{b}_1$ and $\boldsymbol{b}_2$ are the reciprocal lattice vectors, $W(\mathbf{G}_{mn}, j\omega)$ is the plane wave amplitude corresponding to $\mathbf{G}_{mn}$, and $\boldsymbol{k}$ is the Bloch wavevector. Substituting Eq. (68) into Eqs. (66) and (67) yields

$$\sum_{m,n} W(\mathbf{G}_{mn}, j\omega)\left(D^E\|\mathbf{k}+\mathbf{G}_{mn}\|^4 - m_p\omega^2\right)e^{-j(\mathbf{k}+\mathbf{G}_{mn})\cdot\mathbf{P}}$$
$$- \vartheta \sum_{rs} \bar{v}_{rs}\nabla^2 d(\mathbf{P} - \mathbf{P}_{rs}) = 0 \quad (69)$$

$$(j\omega C_p + Y(j\omega))\bar{v}_{rs} + j\omega\vartheta \sum_{m,n} W(\mathbf{G}_{mn}, j\omega)\|\mathbf{k}+\mathbf{G}_{mn}\|^2$$
$$\times \int_D d(\mathbf{P} - \mathbf{P}_{rs})e^{-j(\mathbf{k}+\mathbf{G}_{mn})\cdot\mathbf{P}}dD = 0 \quad (70)$$

where we have used the simplification

$$\nabla^2 e^{-j(\mathbf{k}+\mathbf{G}_{mn})\cdot\mathbf{P}} = \|\mathbf{k}+\mathbf{G}_{mn}\|^2 e^{-j(\mathbf{k}+\mathbf{G}_{mn})\cdot\mathbf{P}} \quad (71)$$
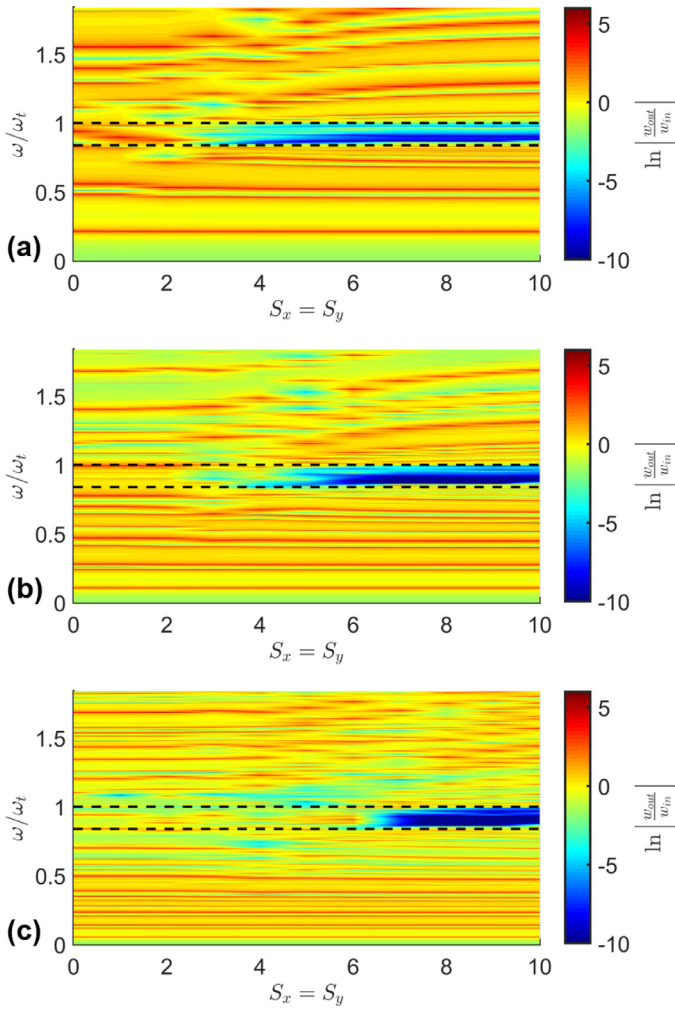
Fig. 3. Plate transmissibility (input at (0.85a, 0.85b) and output at (0.15a, 0.15b)) and resonant frequencies vs. number of electrodes and normalized excitation frequency for (a) $\omega_t = 5\omega_1$, (b) $\omega_t = 10\omega_1$, and (c) $\omega_t = 20\omega_1$ using $N = 900$ plate modes in the expansion. The heatmap shows the plate transmissibility vs. number of electrodes and excitation frequency. Horizontal dashed lines indicate the bandgap predicted by Eq. (61). More electrode segmentation is required to create the locally resonant bandgap at higher frequency ranges (i.e. higher modal neighborhoods).

where $\|\cdot\|$ denotes the Euclidean norm. Note that, since the system is periodic, integrating over the unit cell (r, s) is equivalent to integrating a shifted exponential over unit cell at the origin, i.e.

$$\int_D d(\mathbf{P} - \mathbf{P}_{rs})e^{-j(\mathbf{k}+\mathbf{G}_{mn})\cdot\mathbf{P}}dD = \int_D d(\mathbf{P})e^{-j(\mathbf{k}+\mathbf{G}_{mn})\cdot(\mathbf{P}+\mathbf{P}_{rs})}dD \quad (72)$$

$$= e^{-j(\mathbf{k}+\mathbf{G}_{mn})\cdot\mathbf{P}_{rs}} \int_D d(\mathbf{P})e^{-j(\mathbf{k}+\mathbf{G}_{mn})\cdot\mathbf{P}}dD \quad (73)$$

Using Eq. (70), it can be shown that the above implies

$$\bar{v}_{rs} = e^{-j\mathbf{k}\cdot\mathbf{P}_{rs}}v_0 \quad (74)$$

where $v_0 = \bar{v}_{00}$ is the voltage on the electrode in unit cell (0, 0). Thus, it is only necessary to calculate v_0 to obtain the voltage at every unit cell. Substituting Eq. (74) into (69) gives

$$\sum_{m,n} W(\mathbf{G}_{mn}, j\omega)(D_E\|\mathbf{k}+\mathbf{G}_{mn}\|^4 - m_p\omega^2)e^{-j\mathbf{G}_{mn}\cdot\mathbf{P}}$$
$$- \vartheta v_0 \sum_{r,s} e^{j\mathbf{k}\cdot(\mathbf{P}-\mathbf{P}_{rs})}\nabla^2 d(\mathbf{P} - \mathbf{P}_{rs}) = 0 \quad (75)$$

Note that the summation over r, s forms a periodic function in space, which can be expanded with a Fourier series of the form

$$\sum_{r,s} e^{j\mathbf{k}\cdot(\mathbf{P}-\mathbf{P}_{rs})}\nabla^2 d(\mathbf{P} - \mathbf{P}_{rs}) = \sum_{m,n} \mathscr{D}(\mathbf{G}_{mn})e^{-j\mathbf{G}_{mn}\cdot\mathbf{P}} \quad (76)$$

where

$$\mathscr{D}(\mathbf{G}_{mn}) = \frac{1}{\Delta D}\|\mathbf{k}+\mathbf{G}_{mn}\|^2 \int_{d_0} e^{j(\mathbf{k}+\mathbf{G}_{mn})\cdot\mathbf{P}}dD \quad (77)$$

$$= \frac{1}{\Delta D}\oint_{\partial d_0} \nabla e^{j(\mathbf{k}+\mathbf{G}_{mn})\cdot\mathbf{P}} \cdot \mathbf{n}dS \quad (78)$$

where d_0 indicates the region where $d(\mathbf{P})$ is equal to one (i.e. the electrode of the (0, 0) unit cell), and ΔD is the area of the unit cell. The second form of the coupling integral may be more convenient for electrodes with smoothly parameterized boundaries (e.g., circular electrodes). Summarizing, we have equations

$$W(\mathbf{G}_{mn}, j\omega)\left[D^E\|\mathbf{k}+\mathbf{G}_{mn}\|^4 - m_p\omega^2\right] - \vartheta v_0\mathscr{D}(\mathbf{G}_{mn}) = 0 \quad (79)$$

$$(j\omega + h(j\omega))v_0 + j\omega\frac{\vartheta}{\hat{C}_p}\sum_{m,n} W(\mathbf{G}_{mn}, j\omega)\mathscr{D}^*(\mathbf{G}_{mn}) = 0 \quad (80)$$

where $()^*$ denotes the complex conjugate. It is straightforward to extend these equations to the case of unit cells with multiple non-overlapping electrode pairs with separate shunt circuits. These equations can be solved numerically for the plane wave amplitudes W and voltage v_0 for a given excitation frequency ω and Bloch wavevector $\mathbf{k}$. Alternatively, these equations can be solved for the resonant frequencies ω for $\mathbf{k}$ in the irreducible region of the first Brillouin zone to obtain the dispersion curves of the unit cell. For example, for inductive shunting, we obtain the generalized eigenvalue problem

$$W(\mathbf{G}_{mn}, j\omega)\left[D^E\|\mathbf{k}+\mathbf{G}_{mn}\|^4 - m_p\omega^2\right] - \vartheta v_0\mathscr{D}(\mathbf{G}_{mn}) = 0 \quad (81)$$

$$\left(\omega_t^2 - \omega^2\right)v_0 - \omega^2\frac{\vartheta}{\hat{C}_p}\sum_{m,n} W(\mathbf{G}_{mn}, j\omega)\mathscr{D}^*(\mathbf{G}_{mn}) = 0 \quad (82)$$

or in matrix form,

$$\left(\mathbf{K} - \omega^2\mathbf{M}\right)\mathbf{q} = \mathbf{0} \quad (83)$$

Note that the coupling term $\mathscr{D}(\mathbf{G}_{mn})$ depends on the shape of the electrode in the unit cell. For simple electrode shapes (e.g., rectangular or circular electrodes), this integral can be computed in closed form in terms of the reciprocal lattice point coordinates m and n. This provides a straightforward technique to perform topology optimization, e.g., by discretizing the electrode geometry into a grid of small rectangular electrodes.

4. Numerical validation

To validate the results of Sections 2 and 3, numerical studies were performed using the commercially available finite element software COMSOL Multiphysics. The results are separated into the analysis of a finite plate with free boundaries, to validate the results of Section 2, and the unit-cell based dispersion analysis of an infinite plate, to validate the results of Section 3. Note that the finite element model cannot handle the discontinuities imposed by the assumption of Eq. (28), and so we introduce thin regions at the boundaries of each electrode that are left at open circuit. This allows the voltage to vary smoothly between the voltage level of the electrode and any short-circuit regions on the plate (Fig. 4)
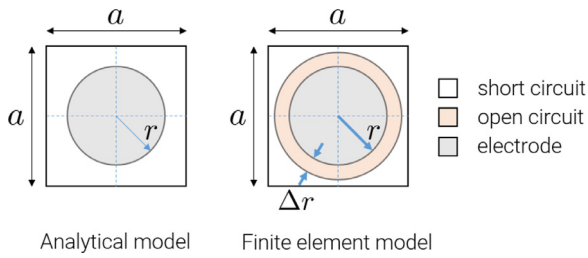
Fig. 4. Schematic showing the differences between the analytical model and finite element model. A thin open circuit region is introduced at the boundary of each electrode to remove the discontinuities in voltage for the finite element model.

4.1. Finite plate

The dimensions and material properties of the plate considered are identical to those in Section 2, but free boundary conditions were used to avoid singularities in the finite element solver. To reduce the model size, it is assumed that the plate is excited at the center, reducing the degrees of freedom by a factor of four using symmetry. The full plate has a 16×14 grid of 4.5cm square electrodes, with 1cm of spacing between adjacent electrodes and 0.5cm between the electrodes and the plate edges. To remove voltage discontinuities, a transition region of width 0.25cm was left at open circuit around each electrode, while the remaining surface of the plate was left at short circuit. Each pair of electrodes was assumed to have constant voltage over its surface, and shunted to an inductance of 5H.
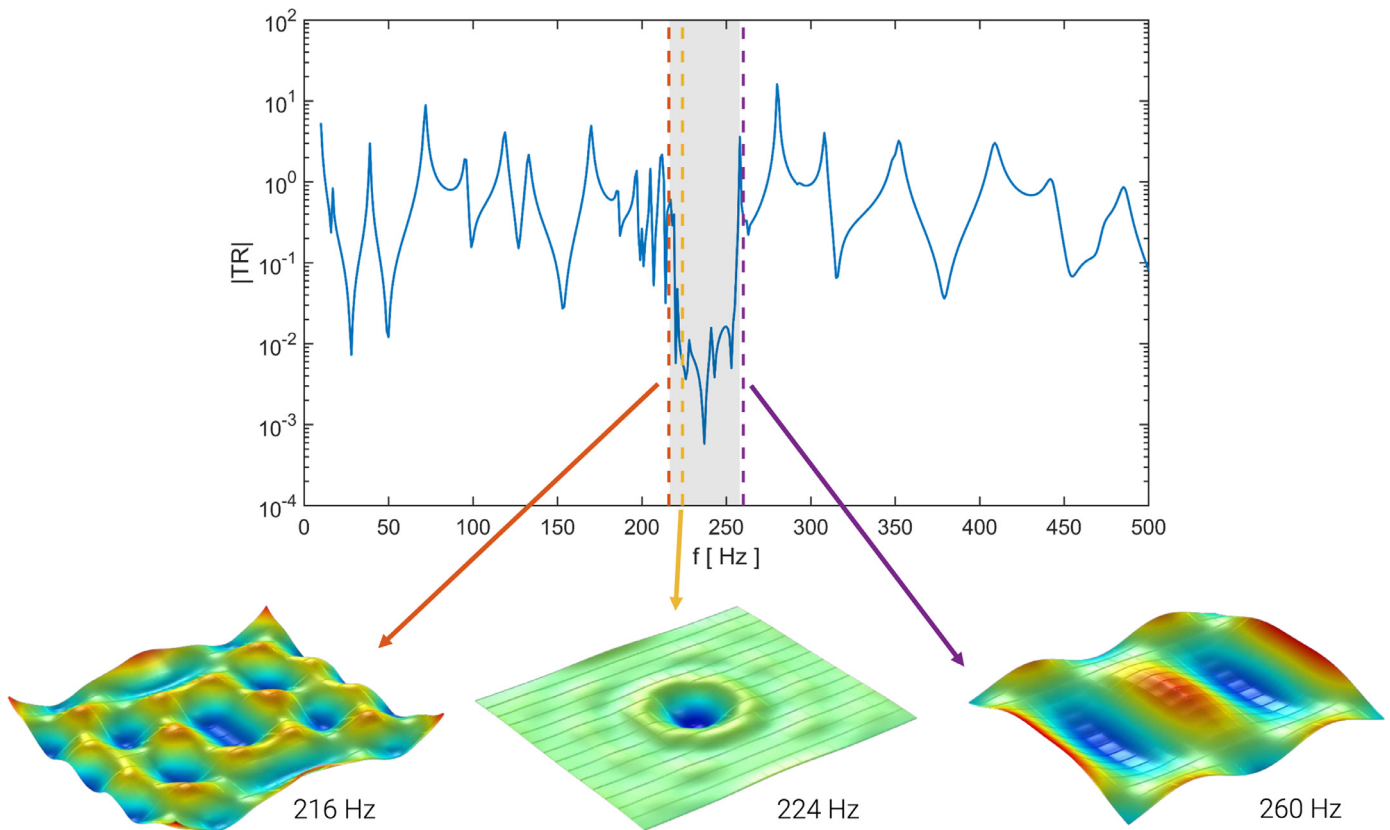
The plate transmissibility at $(x, y) = (15cm, 15cm)$ is shown in Fig. 5. To validate the analytical model, we compare the locally res-

onant bandgap of the finite element model to the bandgap predictions of Eq. (61). The right edge frequency was estimated as 258Hz (the first resonance post-bandgap), yielding a left edge frequency of 216.4Hz. These frequencies are shown by the shaded gray region in Fig. 5, demonstrating that the simplified analytical model can be used to predict the bandgap of the finite element model. Note that the right edge frequency is slightly lower than the predicted value of $f_t = 268Hz$, which can be attributed to fringing effects at the edges of each electrode. Fringing fields would increase the effective piezoelectric capacitance, resulting in a lower-than-predicted shunt resonance.
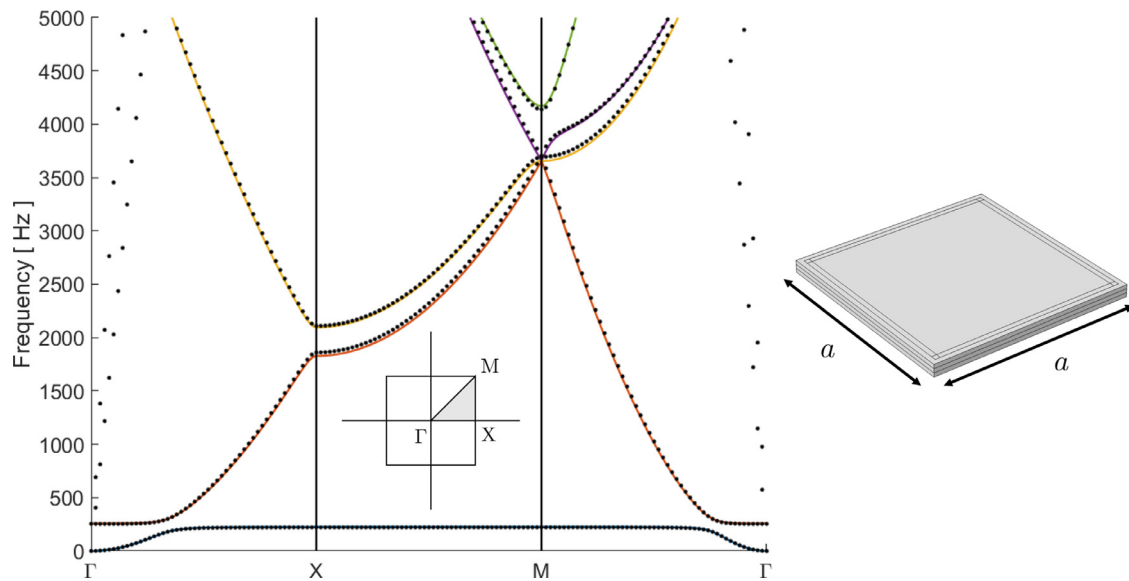
4.2. Unit-cell dispersion analysis

To validate the plane wave expansion method formulated here for bimorph plates, we perform numerical studies using a finite element model of a single unit cell with periodic boundary conditions. We consider a square unit cell of dimensions $a = b = 5cm$, with $h_s = h_p = 1mm$, and an aluminum shim with PZT-5H piezoelectric layers, as in Section 4.1. For the PWE method, a maximum plane wave index of $M = 7$ was used, giving a total of $(2M + 1)^2 + 1 = 226$ degrees of freedom, three orders of magnitude smaller than the finite element model. The dispersion curves for a rectangular and circular electrodes are shown in Figs. 6 and 7, respectively. In both cases, it is clear that there is excellent agreement between the finite element results and the results of analytical model developed here. Both the bandgap edge frequencies and higher frequency modes are predicted well.

Discrepancies between the analytical model and finite element model can be attributed to the assumptions in the analytical model, especially the assumption of zero voltage outside the elec-

Fig. 5. Plate transmissibility at $(x, y) = (15cm, 15cm)$ for an input at $(x, y) = (40cm, 35cm)$ for the finite element model of a bimorph plate. The shaded gray region shows the estimated bandgap using the analytical model, showing good agreement to the finite element model. The insets show the full transverse plate displacement at 216Hz, 224Hz, and 260Hz, i.e. frequencies just before, inside, and just after the locally resonant bandgap, respectively.

Fig. 6. Dispersion curves calculated with the plane wave expansion method (solid lines) and finite element analysis (dots) for a unit cell with a square electrode with length $\Delta x = \Delta y = 0.9a$ centered in the unit cell, with a transition region of thickness $0.025a$. The unit cell geometry is shown on the right. An inductance of 5H was placed between the two electrodes and the central shim.
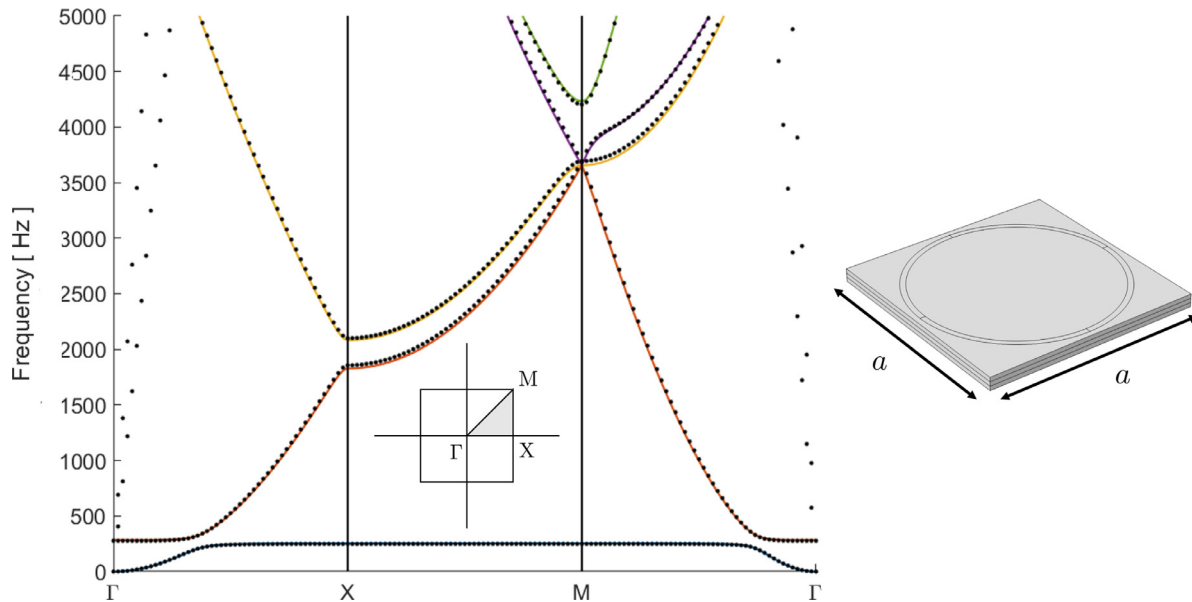
Fig. 7. Dispersion curves calculated with the plane wave expansion method (solid lines) and finite element analysis (dots) for a unit cell with circular electrode with radius $r = 0.45a$ centered in the unit cell, with a transition region of radius $0.025a$. The unit cell geometry is shown on the right. An inductance of 5H was placed between the two electrodes and the central shim.

trode regions of the surface. Although the size of the open circuit transition region in the finite element model was kept relatively small, the effects of fringing fields and the smooth variation in voltage across this region are not accounted for in the analytical model.

5. Conclusions

The fully coupled electromechanical boundary value problem for the transverse vibration and voltage field of a thin piezoelectric bimorph locally resonant metamaterial plate was derived using Hamilton's principle. The governing equations can be used to model bimorph metamaterial plates of any shape with arbitrary electrode segmentation. Further, it was shown that by segmenting the surface of the plate into a sufficient number of discrete electrodes, the effective dynamic stiffness of the bimorph plate is determined solely by the system electromechanical coupling and the shunt admittance applied to each electrode. The edge frequencies of the locally resonant bandgap were obtained in closed form, and the system-level electromechanical coupling was derived in terms of material and geometric parameters. Numerical case studies demonstrated clear convergence to the ideal locally resonant bandgap for a rectangular simply supported plate with a rectangular grid of electrodes. Finally, finite element results validated the simplified analytical model for both the vibration response of a finite plate and dispersion analysis of a single unit cell.

Appendix A. Piezoelectric Constitutive Equations

The constitutive equations for the transversely isotropic piezoelectric layers is given in contracted notation as

$$
\begin{bmatrix} S_1 \\ S_2 \\ S_3 \\ S_4 \\ S_5 \\ S_6 \\ D_1 \\ D_2 \\ D_3 \end{bmatrix} = \begin{bmatrix} s_{11}^E & s_{12}^E & s_{13}^E & 0 & 0 & 0 & 0 & 0 & d_{31} \\ s_{12}^E & s_{11}^E & s_{13}^E & 0 & 0 & 0 & 0 & 0 & d_{31} \\ s_{13}^E & s_{13}^E & s_{33}^E & 0 & 0 & 0 & 0 & 0 & d_{33} \\ 0 & 0 & 0 & s_{55}^E & 0 & 0 & 0 & d_{15} & 0 \\ 0 & 0 & 0 & 0 & s_{55}^E & 0 & d_{15} & 0 & 0 \\ 0 & 0 & 0 & 0 & 0 & s_{66}^E & 0 & 0 & 0 \\ 0 & 0 & 0 & 0 & d_{15} & 0 & \varepsilon_{11}^T & 0 & 0 \\ 0 & 0 & 0 & d_{15} & 0 & 0 & 0 & \varepsilon_{11}^T & 0 \\ d_{31} & d_{31} & d_{33} & 0 & 0 & 0 & 0 & 0 & \varepsilon_{33}^T \end{bmatrix} \begin{bmatrix} T_1 \\ T_2 \\ T_3 \\ T_4 \\ T_5 \\ T_6 \\ E_1 \\ E_2 \\ E_3 \end{bmatrix}
$$

$$(A.1)$$

where s_{ij}^E are the compliance components at constant electric field, d_{ij} are piezoelectric constants, and ε_{ij}^T are the permittivity components at constant stress. Under the assumptions of plane stress (for a thin plate), and assuming voltage is applied through the thickness, such that E_3 is the dominant electric field component, the reduced constitutive equation can be written as

$$
\begin{bmatrix} T_1 \\ T_2 \\ T_6 \\ D_3 \end{bmatrix} = \begin{bmatrix} \bar{c}_{11}^E & \bar{c}_{12}^E & 0 & -\bar{e}_{31} \\ \bar{c}_{12}^E & \bar{c}_{11}^E & 0 & -\bar{e}_{31} \\ 0 & 0 & \bar{c}_{66}^E & 0 \\ \bar{e}_{31} & \bar{e}_{31} & 0 & \bar{\varepsilon}_{33}^S \end{bmatrix} \begin{bmatrix} S_1 \\ S_2 \\ S_6 \\ E_3 \end{bmatrix}
$$

$$(A.2)$$

where

$$
\bar{c}_{11}^E = \frac{s_{11}^E}{\left(s_{11}^E + s_{12}^E\right)\left(s_{11}^E - s_{12}^E\right)}
$$

$$(A.3)$$

$$
\bar{c}_{12}^E = \frac{-s_{12}^E}{\left(s_{11}^E + s_{12}^E\right)\left(s_{11}^E - s_{12}^E\right)}
$$

$$(A.4)$$

$$
\bar{c}_{66}^E = \frac{1}{s_{66}^E} = \frac{1}{2}\left(\bar{c}_{11}^E - \bar{c}_{12}^E\right)
$$

$$(A.5)$$

$$
\bar{e}_{31} = \frac{d_{31}}{s_{11}^E + s_{12}^E}
$$

$$(A.6)$$

$$
\bar{\varepsilon}_{33}^S = \varepsilon_{33}^T - \frac{2d_{31}^2}{s_{11}^E + s_{12}^E}
$$

$$(A.7)$$

where the overbars indicate properties obtained from the full constitutive equations (Eq. (A.1)) under the assumptions of plane stress and voltage applied through the thickness.

Appendix B. Derivation of Governing Equations

B1. Stress and strain

Since the system is symmetric across the central plane of the plate, the mid-plane deformation problem is decoupled from the transverse motion. Under the kinematic assumptions of Kirchhoff plate theory, we consider displacement field

$$
u_1 = -z\frac{\partial w}{\partial x}
$$

$$(B.1)$$

$$
u_2 = -z\frac{\partial w}{\partial y}
$$

$$(B.2)$$

$$
u_3 = w(x, y)
$$

$$(B.3)$$

and corresponding strains

$$
\epsilon_{xx} = -z\frac{\partial^2 w}{\partial x^2}
$$

$$(B.4)$$

$$
\epsilon_{yy} = -z\frac{\partial^2 w}{\partial y^2}
$$

$$(B.5)$$

$$
\epsilon_{xy} = -z\frac{\partial^2 w}{\partial x\partial y}
$$

$$(B.6)$$

We further assume plane stress conditions, such that the constitutive law for the piezoelectric layers is given as in Appendix A. For the isotropic central shim, the stress field in contracted notation is given by

$$
T_1 = -\frac{Ez}{1-\nu_s^2}\left(\frac{\partial^2 w}{\partial x^2} + \nu_s\frac{\partial^2 w}{\partial y^2}\right)
$$

$$(B.7)$$

$$
T_2 = -\frac{Ez}{1-\nu_s^2}\left(\frac{\partial^2 w}{\partial y^2} + \nu_s\frac{\partial^2 w}{\partial x^2}\right)
$$

$$(B.8)$$

$$
T_6 = -\frac{Ez}{1+\nu_s}\frac{\partial^2 w}{\partial x\partial y}
$$

$$(B.9)$$

$$
T_3 = T_4 = T_5 = 0
$$

$$(B.10)$$

B2. Kinetic energy

The kinetic energy of the bimorph plate is

$$
T = \frac{1}{2}\int_{V_s} \rho_s \left(\frac{\partial w}{\partial t}\right)^2 dV_s + \frac{1}{2}\int_{V_p} \rho_p \left(\frac{\partial w}{\partial t}\right)^2 dV_p
$$

$$(B.11)$$

$$
= \frac{1}{2}m\int_D \left(\frac{\partial w}{\partial t}\right)^2 dD
$$

$$(B.12)$$

where

$$
m_p = \rho_s h_s + 2\rho_p h_p
$$

$$(B.13)$$

is the mass per unit area of the bimorph plate. Taking the first variation,

$$
\delta T = \frac{1}{2}m_p \int_D \delta\left(\frac{\partial w}{\partial t}\right)^2 dD
$$

$$
= m_p \int_D \frac{\partial w}{\partial t}\frac{\partial(\delta w)}{\partial t}dD
$$

and integrating w.r.t. time:

$$
\int_{t_1}^{t_2} \delta T dt = m_p \int_D \int_{t_1}^{t_2} \frac{\partial w}{\partial t}\frac{\partial(\delta w)}{\partial t}dt dD
$$

$$
= m_p \int_D \left\{\frac{\partial w}{\partial t}\delta w\Big|_{t_1}^{t_2} - \int_{t_1}^{t_2}\frac{\partial^2 w}{\partial t^2}\delta w dt\right\}dD
$$

$$
= -m_p \int_{t_1}^{t_2}\left[\int_D \frac{\partial^2 w}{\partial t^2}\delta w dD\right]dt
$$

B3. Electromechanical potential

The total contribution to the potential energy from the central layer is

$$
U_s = \frac{1}{2}\int_{V_s} \sigma_{ij}\epsilon_{ij}dV_s
$$

$$(B.14)$$

$$
= \frac{D_s}{2}\int_D \left\{\left[\left(\frac{\partial^2 w}{\partial x^2}\right)^2 + 2\nu_s\frac{\partial^2 w}{\partial x^2}\frac{\partial^2 w}{\partial y^2} + \left(\frac{\partial^2 w}{\partial y^2}\right)^2\right]\right.
$$

$$
\left. + 2(1-\nu_s)\left(\frac{\partial^2 w}{\partial x\partial y}\right)^2\right\}dD
$$

$$(B.15)$$

where

$$D_s = \frac{E}{1 - \nu_s^2} \int_{-h_s/2}^{h_s/2} z^2 dz = \frac{E}{1 - \nu_s^2} \frac{z^3}{3}\Big|_{-h_s/2}^{h_s/2} = \frac{Eh_s^3}{12(1 - \nu_s^2)} \quad (B.16)$$

is the flexural rigidity contribution from the central shim. For the piezoelectric layers, we have electrical enthalpy

$$H_p = \frac{1}{2}\int_{V_p} (U - E_i D_i) dV_p \quad (B.17)$$

$$= \frac{1}{2}\int_{V_p} \Big(\bar{c}_{11}^E S_1^2 + 2\bar{c}_{12}^E S_1 S_2 + \bar{c}_{11}^E S_2^2 + \bar{c}_{66}^E S_6^2 + \bar{e}_{31} E_3 S_1 + \bar{e}_{31} E_3 S_2 - \bar{\varepsilon}_{33}^S E_3^2\Big) dV_p \quad (B.18)$$

$$= \frac{D_p}{2}\int_D \left\{\left[\left(\frac{\partial^2 w}{\partial x^2}\right)^2 + \left(\frac{\partial^2 w}{\partial y^2}\right)^2\right] + 2\frac{\bar{c}_{12}^E}{\bar{c}_{11}^E}\frac{\partial^2 w}{\partial x^2}\frac{\partial^2 w}{\partial y^2} + 4\frac{\bar{c}_{66}^E}{\bar{c}_{11}^E}\left(\frac{\partial^2 w}{\partial x \partial y}\right)^2\right\} dD + \int_D \left[\vartheta v \nabla^2 w + \frac{\hat{C}_p}{2}v^2\right] dD \quad (B.19)$$

where it has been assumed that $E_3 = \pm v(\mathbf{P}, t)/h_p$ (i.e. uniform electric field) in the top and bottom piezoelectric layers respectively,

$$D_p = \bar{c}_{11}^E\left(\frac{1}{6}h_p\left(4h_p^2 + 6h_p h_s + 3h_s^2\right)\right) \quad (B.20)$$

is the effective flexural rigidity contribution of the piezoelectric layers, and

$$\vartheta = \bar{e}_{31}(h_s + h_p) \quad (B.21)$$

$$\hat{C}_p = \frac{2\bar{\varepsilon}_{33}}{h_p} \quad (B.22)$$

are the coupling parameter in physical coordinates and effective piezoelectric capacitance per area. Note there are no assumptions yet on the voltage distribution $v(\mathbf{P}, t)$. In summary, the total electrical enthalpy can be written as

$$H = \frac{1}{2}\int_D \left\{(D_s + D_p)\left[\left(\frac{\partial^2 w}{\partial x^2}\right)^2 + \left(\frac{\partial^2 w}{\partial y^2}\right)^2\right] + 2\left(D_p\frac{\bar{c}_{12}^E}{\bar{c}_{11}^E} + D_s \nu_s\right)\frac{\partial^2 w}{\partial x^2}\frac{\partial^2 w}{\partial y^2} + 2\left(D_p\frac{2\bar{c}_{66}^E}{\bar{c}_{11}^E} + D_s(1 - \nu_s)\right)\left(\frac{\partial^2 w}{\partial x \partial y}\right)^2 - 2\left[\vartheta v \nabla^2 w + \frac{\hat{C}_p}{2}v^2\right]\right\} dD \quad (B.23)$$

Taking the first variation,

$$\delta H = \int_D \left\{(D_s + D_p)\left(\nabla^4 w \delta w + \nabla \cdot (\nabla^2 w \nabla(\delta w) - \delta w \nabla \nabla^2 w)\right) - D^E(1 - \nu)\nabla \cdot \Phi \nabla(\delta w) - \left[\vartheta\left(\nabla^2 w \delta v + \delta w \nabla^2 v + \nabla \cdot (v \nabla(\delta w) - \delta w \nabla v)\right)\right] + \hat{C}_p v \delta v\right\} dD \quad (B.24)$$

where

$$\Phi = \begin{bmatrix} w_{yy} & -w_{xy} \\ -w_{xy} & w_{xx} \end{bmatrix}$$

where we used the identity

$$\nabla \cdot (f\nabla g - g\nabla f) = f\nabla^2 g - g\nabla^2 f$$

with $f = \nabla^2 w$, $g = \delta w$, and with $f = v$, $g = \delta w$. By applying the divergence theorem, the divergence terms only affect the system's boundary conditions. Thus, we separate the divergence terms out as

$$\delta H = \int_D \left\{\left[D^E \nabla^4 w - \vartheta \nabla^2 v\right]\delta w - \left[\vartheta \nabla^2 w + \hat{C}_p v\right]\delta v\right\} dD + \oint_{\partial D}\left\{\left(D^E \nabla^2 w - D^E(1 - \nu)\Phi - \vartheta v\right)\nabla(\delta w) + \left(-D_E \nabla \nabla^2 w + \vartheta \nabla v\right)\delta w\right\} \cdot \mathbf{n}dS \quad (B.25)$$

B4. Virtual work

Work is done either through external current or force applied to the piezoelectric plate. Thus,

$$\delta W_{nc} = \int_D f(\mathbf{P}, t)\delta w(\mathbf{P}, t)dD + \int_D Q(\mathbf{P}, t)\delta v(\mathbf{P}, t)dD$$

$$= \int_D f(\mathbf{P}, t)\delta w(\mathbf{P}, t)dD - \int_D \left[\int_{t_0}^t J(\mathbf{P}, \tau)\delta v(\mathbf{P}, \tau)d\tau\right] dD$$

where $J(\mathbf{P}, t)$ is the current density flowing *out of* the electrodes of the bimorph *into* the central shim

B5. Boundary conditions

Boundary terms arise only from the electrical enthalpy, since we have no added mass contributions. Define moments and shear as

$$M_x = -D^E w_{xx} - D^E \nu w_{yy} \quad (B.26)$$

$$M_y = -D^E w_{yy} - D^E \nu w_{xx} \quad (B.27)$$

$$M_{xy} = -(D_E - D_\nu)w_{xy} \quad (B.28)$$

$$Q_x = \frac{\partial M_x}{\partial x} + \frac{\partial M_{xy}}{\partial y} = -D_E(w_{xxx} - w_{xyy}) \quad (B.29)$$

$$Q_y = \frac{\partial M_y}{\partial y} + \frac{\partial M_{xy}}{\partial x} = -D_E(w_{yyy} - w_{xxy}) \quad (B.30)$$

Then we have

$$\left[D^E \nabla^2 w - D^E(1 - \nu)\Phi\right]\nabla(\delta w) \cdot \mathbf{n} = -\begin{bmatrix} M_x \delta w_x + M_{xy} \delta w_y \\ M_{xy} \delta w_x + M_y \delta w_y \end{bmatrix} \cdot \mathbf{n} \quad (B.31)$$

Transform to normal and tangent components to the boundary via rotation by an angle ϕ:

$$dx = -ds\sin\phi, \quad dy = ds\cos\phi \quad (B.32)$$

and

$$\frac{\partial}{\partial x} = \cos\phi\frac{\partial}{\partial n} - \sin\phi\frac{\partial}{\partial s} \quad (B.33)$$

$$\frac{\partial}{\partial y} = \sin\phi\frac{\partial}{\partial n} + \cos\phi\frac{\partial}{\partial s} \quad (B.34)$$

Then the normal vector $\mathbf{n}$ is given by

$$\mathbf{n} = \begin{bmatrix} \cos\phi \\ \sin\phi \end{bmatrix} \quad (B.35)$$

and

$$\delta w_x = \delta w_n \cos\phi - \delta w_s \sin\phi \quad (B.36)$$

$$\delta w_y = \delta w_n \sin\phi + \delta w_s \cos\phi \tag{B.37}$$

We can then rewrite the moment term in Eq. (B.31) as

$$\begin{bmatrix} M_x \delta w_x + M_{xy} \delta w_y \\ M_{xy} \delta w_x + M_y \delta w_y \end{bmatrix} \cdot \mathbf{n} = M_n \delta w_n + M_{ns} \delta w_s \tag{B.38}$$

The voltage term simplifies more easily as

$$\vartheta v \nabla(\delta w) \cdot \mathbf{n} = \vartheta v \delta w_n \tag{B.39}$$

Overall, the boundary integrals are then

$$0 = \oint_{\partial D} \{ (-M_n - \vartheta v)\delta w_n - M_{ns}\delta w_s $$
$$ + \left(-D_E \frac{\partial}{\partial n}\nabla^2 w + \vartheta \frac{\partial v}{\partial n} \right)\delta w \} dS \tag{B.40}$$

Next, we integrate by parts to remove the extra boundary condition:

$$\oint_{\partial D} M_{ns} \frac{\partial(\delta w)}{\partial s} dS = M_{ns}\delta w \Big|_{\partial D} - \oint_{\partial D} \frac{\partial M_{ns}}{\partial s}\delta w dS \tag{B.41}$$

Note that the term $M_{ns}\delta w|_{\partial D}$ is responsible for the "corner condition," which is unchanged by the voltage coupling. Assuming the term vanishes, we have boundary integral

$$0 = \oint_{\partial D} \left\{ (-M_n - \vartheta v)\delta w_n + \left(\frac{\partial M_{ns}}{\partial s} - D_E \frac{\partial}{\partial n}\nabla^2 w + \vartheta \frac{\partial v}{\partial n} \right)\delta w \right\} dS \tag{B.42}$$

and so we have boundary conditions summarized as:

$$\text{either} \quad w = 0 \quad \text{on} \quad \partial D \tag{B.43}$$

$$\text{or} \quad \frac{\partial M_{ns}}{\partial s} - D_E \frac{\partial}{\partial n}\nabla^2 w + \vartheta \frac{\partial v}{\partial n} = 0 \quad \text{on} \quad \partial D \tag{B.44}$$

$$\text{and either} \quad \frac{\partial w}{\partial n} = 0 \quad \text{on} \quad \partial D \tag{B.45}$$

$$\text{or} \quad M_n + \vartheta v = 0 \quad \text{on} \quad \partial D \tag{B.46}$$

The voltage coupling contributes to both the natural boundary conditions, as voltage on the boundary applies a moment and contributes to the effective shear.

B6. Domain equations

Substituting into Hamilton's Principle and removing the boundary terms:

$$0 = \int_{t_1}^{t_2} (\delta T - \delta U + \delta W_{nc})\,dt $$
$$ = \int_{t_1}^{t_2} \left\{ \int_D \left[-m_p \frac{\partial^2 w}{\partial t^2} - D^E \nabla^4 w + \vartheta \nabla^2 v + f(\mathbf{P}, t) \right]\delta w \, dD \right. $$
$$ \left. + \int_D \left[\vartheta \nabla^2 w + \hat{C}_p v - \int_{t_0}^{t} J(\mathbf{P}, \tau)\,d\tau \right]\delta v\,dD \right\}dt $$

Since this equation must be satisfied for any δw and δv as well as any t_1 and t_2, we can obtain the governing equations as

$$D^E \nabla^4 w(\mathbf{P}, t) + m_p \frac{\partial^2 w(\mathbf{P}, t)}{\partial t^2} - \vartheta \nabla^2 v(\mathbf{P}, t) = f(\mathbf{P}, t) \tag{B.47}$$

$$\hat{C}_p \frac{\partial v(\mathbf{P}, t)}{\partial t} + \vartheta \frac{\partial}{\partial t}\nabla^2 w(\mathbf{P}, t) = J(\mathbf{P}, t) \tag{B.48}$$

References

Arafa, M., Baz, A., 2000. Dynamics of active piezoelectric damping composites. Compos. Part B 31 (4), 255–264.

Aridogan, U., Basdogan, I., Erturk, A., 2014. Analytical modeling and experimental validation of a structurally integrated piezoelectric energy harvester on a thin plate. Smart Mater. Struct. 23 (4), 045039.

Bailey, T., Hubbard Jr., J., 1985. Distributed piezoelectric-polymer active vibration control of a cantilever beam. J. Guidance 8 (5), 605–611.

Casadei, F., Ruzzene, M., Dozio, L., Cunefare, K.A., 2010. Broadband vibration control through periodic arrays of resonant shunts: experimental investigation on plates. Smart Mater. Struct. 19, 015002.

Chen, Y., Hu, G., Huang, G., 2017. A hybrid elastic metamaterial with negative mass density and tunable bending stiffness. J. Mech. Phys. Solids 105, 179–198.

Chen, Y.Y., Huang, G.L., Sun, C.T., 2014. Band gap control in an active elastic metamaterial with negative capacitance piezoelectric shunting. J. Vib. Acoust. 136, 061008.

De Marneffe, B., Preumont, A., 2008. Vibration damping with negative capacitance shunts: theory and experiment. Smart Mater. Struct. 17 (3), 035015.

De Marqui, J.C., Erturk, A., Inman, D.J., 2009. An electromechanical finite element model for piezoelectric energy harvester plates. J. Sound Vib. 327 (1–2), 9–25.

Dimitriadis, E.K., Fuller, C.R., Rogers, C.A., 1991. Piezoelectric actuators for distributed vibration excitation of thin plates. J. Vib. Acoust. 113 (1), 100–107.

Dosch, J.J., Inman, D.J., Garcia, E., 1992. A self-sensing piezoelectric actuator for collocated control. J. Intell. Mater. Syst. Struct. 3, 166–185.

Erturk, A., Inman, D.J., 2009. An experimentally validated bimorph cantilever model for piezoelectric energy harvesting from base excitations. Smart Mater. Struct. 18 (2), 025009.

Fleming, A.J., Behrens, S., Moheimani, S.O.R., 2002. Optimization and implementation of multimode piezoelectric shunt damping systems. IEEE/ASME Trans. Mechatron. 7 (1), 87–94.

Fleming, A.J., Moheimani, S.O.R., 2004. Control orientated synthesis of high-performance piezoelectric shunt impedances for structural vibration control. IEEE Trans. Control Syst. Technol. 13 (1), 98–112.

Forward, R.L., 1979. Electronic damping of vibrations in optical structures. Appl. Opt. 18 (5), 690–697.

Hagood, N.W., von Flotow, A., 1991. Damping of structural vibrations with piezoelectric materials and passive electrical networks. J. Sound Vib. 146 (2), 243–268.

He, X.Q., Ng, T.Y., Sivashanker, S., Liew, K.M., 2001. Active control of FGM plates with integrated piezoelectric sensors and actuators. Int. J. Solids Struct. 38 (9), 1641–1655.

Heyliger, P., Saravanos, D.A., 1995. Exact free-vibration analysis of laminated plates with embedded piezoelectric layers. J. Acoust. Soc. Am. 98 (3), 1547–1557.

Kim, S., Clark, W.W., Wang, Q.-M., 2005. Piezoelectric energy harvesting with a clamped circular plate: analysis. J. Intell. Mater Syst. Struct. 16 (10), 847–854.

Lee, C.K., 1990. Theory of laminated piezoelectric plates for the design of distributed sensors/actuators. part i: governing equations and reciprocal relationships. J. Acoust. Soc. Am. 87 (3), 1144–1158.

Li, X., Chen, Y., Hu, G., Huang, G., 2018. A self-adaptive metamaterial beam with digitally controlled resonators for subwavelength broadband flexural wave attenuation. Smart Mater. Struct. 27 (4), 045015.

Meirovitch, L., 1997. Principles and Techniques of Vibrations. Prentice-Hall, Inc., Upper Saddle River, NJ.

Mindlin, R.D., 1972. High frequency vibrations of piezoelectric crystal plates. Int. J. Solids Struct. 8 (7), 895–906.

Mitchell, J.A., Reddy, J.N., 1995. A refined hybrid plate theory for composite laminates with piezoelectric laminae. Int. J. Solids Struct. 32 (16), 2345–2367.

Moheimani, S., Fleming, A.J., Behrens, S., 2004. Dynamics, stability, and control of multivariable piezoelectric shunts. IEEE/ASME Trans. Mechatron. 9 (1), 87–99.

Niederberger, D., Fleming, A., Moheimani, S.O.R., Morari, M., 2004. Adaptive multimode resonant piezoelectric shunt damping. Smart Mater. Struct. 13 (5), 1025.

Park, C.H., Baz, A., 2005. Vibration control of beams with negative capacitive shunting of interdigital electrode piezoceramics. Modal Anal. 11 (3), 331–346.

Preumont, A., Marneffe, B.D., Krenk, S., 2008. Transmission zeros in structural control with collocated multi-input/multi-output pairs. J. Guidance Control Dynamics 31 (2), 428–432.

Qiu, Z.-c., Zhang, X.-m., Wu, H.-x., Zhang, H.-h., 2007. Optimal placement and active vibration control for piezoelectric smart flexible cantilever plate. J. Sound Vib. 301 (3–5), 521–543.

Saravanos, D.A., Heyliger, P.R., Hopkins, D.A., 1997. Layerwise mechanics and finite element for the dynamic analysis of piezoelectric composite plates. Int. J. Solids Struct. 34 (3), 359–378.

Sheng-Bing, C., Ji-Hong, W., Gang, W., Xi-Sen, W., 2013. Tunable band gaps in acoustic metamaterials with periodic arrays of resonant shunted piezos. Chin. Phys. B 22 (7), 074301.

Sugino, C., Leadenham, S., Ruzzene, M., Erturk, A., 2017. An investigation of electroelastic bandgap formation in locally resonant piezoelectric metastructures. Smart Mater. Struct. 26 (5), 055029.

Sugino, C., Ruzzene, M., Erturk, A., 2018. Design and analysis of piezoelectric metamaterial beams with synthetic impedance shunt circuits. IEEE/ASME Trans. Mechatron 23 (5), 2144–2155.

Tang, J., Wang, K.-W., 2001. Active-passive hybrid piezoelectric networks for vibration control: comparisons and improvement. Smart Mater. Struct. 10 (4), 794.

Tiersten, H.F., 2013. Linear piezoelectric plate vibrations: Elements of the linear theory of piezoelectricity and the vibrations piezoelectric plates. Springer.

Wang, Q., Quek, S.T., Sun, C.T., Liu, X., 2001. Analysis of piezoelectric coupled circular plate. Smart Mater. Struct. 10 (2), 229.

Yu, H., Wang, K.W., 2009. Vibration suppression of mistuned coupled-blade-disk systems using piezoelectric circuitry network. J. Vib. Acoust. 131, 021008.

Zhang, H., Wen, J., Xiao, Y., Wang, G., Wen, X., 2015. Sound transmission loss of metamaterial thin plates with periodic subwavelength arrays of shunted piezo-electric patches. J. Sound Vib. 343, 104–120.

Zhong, Z., Shang, E.T., 2003. Three-dimensional exact analysis of a simply supported functionally gradient piezoelectric plate. Int. J. Solids Struct. 40 (20), 5335–5352.